Journal of Membrane Science 331 (2009) 117–125

Contents lists available at ScienceDirect

Journal of Membrane Science

journal homepage: www.elsevier.com/locate/memsci

Heat transfer in vacuum membrane distillation: Effect of velocity slip

Guy Ramon, Yehuda Agnon*, Carlos Dosoretz

Department of Civil and Environmental Engineering, Technion-Israel Institute of Technology, Haifa 32000, Israel

ARTICLE INFO

Article history:
Received 28 November 2008
Received in revised form 15 January 2009
Accepted 16 January 2009
Available online 23 February 2009

Keywords:
Vacuum membrane distillation
Heat transfer
Slip flow
Temperature polarization
Boundary layer integral method

ABSTRACT

A two-dimensional, boundary layer model is presented, for describing the heat transfer in the feed channel of a vacuum membrane distillation (VMD) module. The model formulation allows for variations of viscosity with temperature, and introduces an 'effective' slip coefficient so as to account for the possible deviation of the flow and heat transfer characteristics over a liquid–gas interface, from those at a solid surface. The model solution provides the temperature field in the feed channel and its dependence on the bulk velocity and temperature, as well as the vapor mass flux across the membrane. While the effect of a temperature variable viscosity becomes increasingly apparent at higher temperatures, its effect on the evaporation mass flux is not substantial. The relative contribution of transverse convection to the evaporation mass flux is shown to be insignificant, within the range of parameters examined. In the presence of an 'effective' velocity slip, the degree of temperature polarization is reduced and a corresponding increase in the evaporation mass flux is observed. Calculated results are in good agreement with experimental data. The presented results suggest that the effect of alternating solid and gas interfaces, encountered by the fluid, on the flow field and resulting heat transfer, should be accounted for if accurate predictions are to be made.

1. Introduction

Membrane distillation (MD) is a process by which vapor is extracted from a liquid stream, through the pores of a membrane capable of sustaining a gas–liquid interface. The feed components evaporate at this interface according to the local vapor–liquid equilibrium and are transported through the pore space driven by a gradient in partial pressure maintained across the membrane. In the case of an aqueous, ionic solution, the evaporating species is the water, and the membrane used is hydrophobic in nature; this prevents the water from entering the membrane pores up to the so-called liquid entry pressure [1]. The MD process has several potentially advantageous features: being based on phase change, it is possible for the process to operate at solution osmotic pressures which normally limit pressure driven membrane separation; in fact, it has been shown that considerable fluxes may be achieved even from saturated brine solutions [2,3]. This feature makes MD a particularly attractive alternative for inland desalination (brackish or waste-water), where high recoveries are crucial for maintaining small discharge volumes. Another noteworthy advantage of the process is its ability to operate at temperatures well below the boiling point, enabling the use of solar heating as the energy source [4,5].

Several configurations have thus far been employed for the process [1], perhaps the simplest of which is direct contact MD (DCMD), where a hot feed and cold distillate are both in contact with the membrane surface, creating a vapor pressure gradient due to the temperature difference across the membrane. The main drawback of this configuration is the irreversible conductive heat loss through the membrane, particularly where thin membranes are used for reducing the resistance to mass transfer. In order to minimize the parasitic heat loss through the membrane, alternative configurations have been proposed whereby a gas phase replaces the cold distillate on the permeate side of the membrane: in air gap MD (AGMD), an air gap on the permeate side separates the membrane from a cold plate on which the vapor condenses; in sweep gas MD – a strip gas (such as dry/cold air) is circulated on the distillate side of the membrane; finally, in vacuum MD (VMD) – a vacuum is applied to the permeate space for extraction of the vapor. The AGMD configuration has the advantage of potential internal heat recovery, while in SGMD and VMD the vapor and latent heat must be recovered externally. However, the VMD configuration benefits from a low resistance to mass transfer within the membrane as well as the ability to operate at lower temperatures.

The evaporation of water at the feed side membrane interface results in a simultaneous reduction of the temperature and increase of the solute concentration, referred to as temperature and concentration polarization, respectively. Conversely, in the DCMD configuration, the permeate side membrane surface temperature will be higher than the bulk temperature, due to the

* Corresponding author. Tel.: +972 4 8292489.
E-mail address: agnon@tx.technion.ac.il (Y. Agnon).

0376-7388/$ – see front matter © 2009 Elsevier B.V. All rights reserved.
doi:10.1016/j.memsci.2009.01.022

condensation of the vapor. Temperature polarization has a much more dramatic impact on MD performance, since the vapor pressure is, in general, more strongly dependent on the temperature than on the solute concentration. Therefore, considerable efforts have been made to model and quantify heat transfer phenomena in the various configurations. For the most part, film theory has been used, supplemented by a variety of heat transfer correlations (see, for example, [6–10]). This approach allows a relatively simple analysis and even provides analytical expressions under certain assumptions [1]. However, employing such an approach neglects the axial variation of the temperature field; moreover, care should be exercised when employing heat transfer correlations which were derived for solid, constant temperature surfaces. Two-dimensional, numerical models, have been formulated for describing AGMD systems [11–13], and have succeeded in illustrating the axial variations of the temperature field and mass flux, as well as their dependence upon various process parameters; however, only the conjugate model presented by Alklaibi and Lior [11] was validated, showing good agreement with experimental data.

In most theoretical models of the MD process, liquid properties are assumed to be constant and their variations with temperature are neglected. However, while the variations in conductivity and/or latent heat are rather small, variations in viscosity may be much more substantial (for example, between 60 and 65 °C, the change in the value of the conductivity, latent heat and viscosity is 0.7%, 0.5% and 7.6%, respectively [14]). In DCMD, it is often observed that the flux is limited by heat transfer in the feed side, even when conditions in the permeate side are identical (see, for example, [15]). This may be attributed to the decrease(increase) in viscosity at the hot(cold) interface, which directly affects the convective heat transfer efficiency. Heat transfer correlations often include a correction factor to account for viscosity variations, and this is sometimes used in the analysis of heat transfer in MD modules (see, for example, [16]); however, it is more commonly assumed that these variations are negligible.

A major difference between MD and other membrane separation processes stems from the role of the membrane. The membranes used in MD are not selective, in the classical sense, but have the sole purpose of supporting a liquid–gas interface, where the evaporation takes place. As already mentioned, for aqueous solutions this is achieved by employing membranes composed of hydrophobic materials. The fluid flowing in a conduit confined by a hydrophobic membrane encounters, in effect, alternating patches of either a liquid–solid interface (at the membrane surface) or a gas–liquid interface (where the membrane pore supports such an interface). In hydrodynamic terms, this means that the boundary condition imposed on the momentum balance equations is either no-slip ($u = 0$, vanishing tangential velocity) at the solid–liquid interface or, to a first approximation, no-shear ($\tau_w = 0$, vanishing shear stress) at the gas–liquid interface (see Fig. 1 for a schematic illustration). The bulk effect may be viewed as a reduced contact area between the fluid and the solid membrane material, which alters the velocity field. In fact, recent studies have shown that nano- and micro-structured hydrophobic surfaces (also termed super-hydrophobic surfaces), possessing a tailored surface roughness in the form of posts or grooves, produce the net effect of reducing the drag force experienced by the liquid flowing over them. This effect is attributed to the fact that on the patterned surface, patches of gas–liquid interfaces are formed, supported by the liquid's surface tension. These surfaces and their functionality possess a striking resemblance to the membranes used in the MD process, and it is therefore plausible that the observed effects are analogous as well.

While the microscopic details of the flow field over such surfaces are difficult to predict quantitatively, it is possible to formulate a macroscopic description by introducing an 'effective' slip parameter, which accounts for the deviations of the flow field from the no-slip case. A simple model of velocity slip dates back to Navier [17], who proposed a linear shear-rate dependence of the velocity, which may be stated in the following form:

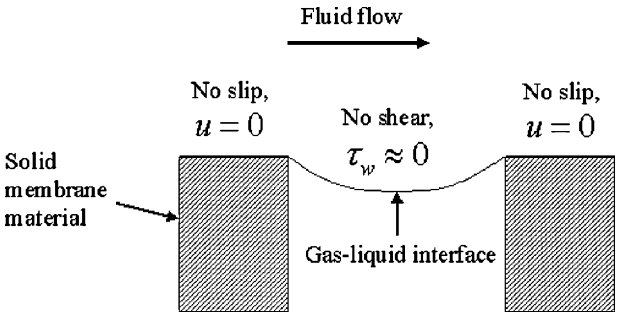

Fig. 1. Schematic illustration of alternating boundary conditions at the membrane surface. At a solid–liquid interface (the membrane material), a no-slip condition is imposed; at the gas–liquid interface (membrane pore), the boundary condition may be approximated as that of a vanishing shear stress.

$$u(y = 0) = l\frac{\partial u}{\partial y}|_{y=0} \tag{1}$$

The model assumes that there exists a constant slip length, l, which can be simply described as the imaginary distance within the solid where the velocity extrapolates to zero.

Experiments conducted with such super-hydrophobic surfaces, under a variety of length scales and flow conditions, have measured slip velocities ranging between 10 and 17% of the mean velocity [18–20], resulting in a drag reduction as high as ~40% [21]. Slip lengths of up to ~30% of the channel height have also been measured [22]. Most importantly, the velocity over the gas–liquid interface has been found to be as much as 51% of the mean velocity [20]. As previously mentioned, the drag reduction effect is attributed to a reduced solid–liquid contact area, and is thus dependent upon the surface porosity. In the described experimental studies [22,21], surface porosity was estimated as ~50%; while data on the surface porosity of membranes used in MD is somewhat scarce, values of ~22–46% have been reported [23], and it is possible to find commercial micro-porous hydrophobic membranes (polypropylene, PVDF), with reported surface porosities greater than 50%. Regardless of the exact value of the surface porosity, it is particularly important to bear in mind that it is the flow over the gas–liquid interface which is expected to have the greatest impact on the MD process. The resulting alteration of the flow field would certainly influence the convective heat transfer characteristics and, consequently, temperature polarization.

It is therefore the purpose of this study to present a theoretical, two-dimensional model of the heat transfer in the feed channel of a VMD module. The temperature dependence of the viscosity is included, as well as the possible existence of an 'effective' slip arising from a reduced contact area of the liquid–solid interface. The paper is organized as follows: Section 2 describes the model formulation and solution methodology, while in Section 3 results are presented and discussed. Finally, Section 4 contains a summary and concluding remarks.

2. Model formulation

We consider a vacuum membrane distillation (VMD) process, depicted schematically in Fig. 2. The evaporation at the membrane pores is driven by a vapor pressure difference across the membrane, maintained by a vacuum applied to the permeate space. The steady-state energy balance in the feed channel boundary layer, assuming that viscous heating effects may be neglected, may be written as

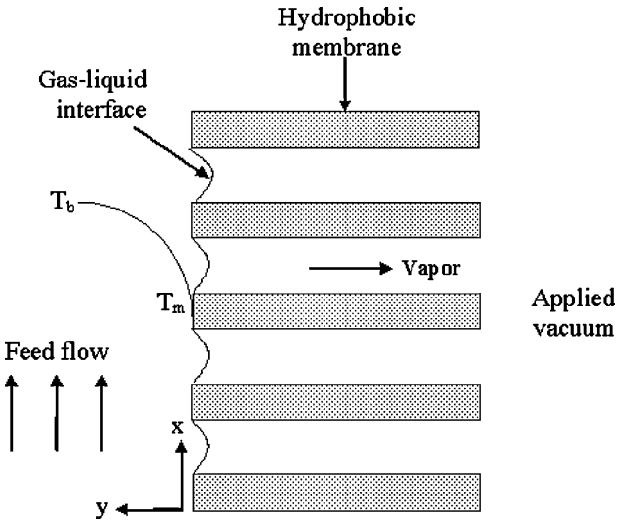

Fig. 2. Schematic drawing of vacuum driven membrane distillation.

follows [25]:

$$u\frac{\partial T}{\partial x} + v\frac{\partial T}{\partial y} = K\frac{\partial^2 T}{\partial y^2} \tag{2}$$

where x and y denote the axial and transverse coordinates, respectively, T is the temperature, u is the axial velocity, v is the transverse velocity and K is the thermal diffusivity of the feed fluid, assumed to be independent of the temperature.

For a steady-state evaporation at the gas–liquid interface, continuity requires that [24]:

$$\vec{V}\cdot\hat{n} = j/\rho \tag{3}$$

where $\vec{V}$ is the velocity vector, $\hat{n}$ is the unit vector normal to the interface, j is the evaporation mass flux and ρ is the liquid density. The interface will likely deflect into the pore under the influence of the pressure in the liquid; however, this deflection should be small for reasonable pressure gradients in the feed channel [21]. Assuming, for simplicity, that the interface is flat, Eq. (3) states that the evaporation mass flux is exactly balanced by the induced transverse velocity, v. Since the evaporation mass flux in MD operation is normally on the order of $\sim$10 kg/m^2 h, the induced transverse velocity is typically quite small, $v \approx 10^{-5} - 10^{-6}$ m/s. The resulting heat flux, however, may still be significant, particularly at high temperatures; moreover, the presence of this heat flux is one of the factors not taken into account in most heat transfer correlations. At this point, it is worthwhile noting the difference between the cause of the polarization phenomena in MD compared to pressure driven membrane filtration. In the latter, polarization is caused by the transverse component of the velocity, as it induces a convective transport of material, which is subsequently rejected by the membrane and accumulates. Conversely, in MD it is the evaporation at the interface which induces the flow, as stated by Eq. (3). Polarization therefore occurs due to a local decrease(increase) in the temperature(concentration) and not by a convective mechanism. In fact, the induced transverse convection in MD acts so as to lower the polarization, by transporting heat from the bulk to the interface.

Within the temperature boundary layer, the velocity field is simplified employing the so-called Lèvêque approximation, where a linear distribution is assumed in the transverse direction. Although strictly valid for the entrance region or large Prandtl numbers ($Pr = \nu/K$), this approximation has been used successfully in describing heat transfer for a wide range of fluids and configurations [25]. Modified by the use of the Navier slip condition, Eq. (1), the velocity distribution may be written as:

$$u = \dot{\gamma}\left(\frac{l_0 d_h}{2} + y\right) \tag{4}$$

with $\dot{\gamma}$, the shear rate, expressed as:

$$\dot{\gamma} = \frac{\tau_w}{\mu_m} = \frac{8U\mu_b}{d_h\mu_m} \tag{5}$$

where U is the bulk velocity, d_h is the hydraulic diameter, μ_b, μ_m denote the viscosities in the bulk fluid and at the membrane surface, respectively, and $l_0 = 2l/d_h$ is the slip length, scaled by half the hydraulic diameter (for a cylindrical tube this is equivalent to the radius). In this boundary layer formulation, the geometry of the system is prescribed through the hydraulic diameter, d_h. The velocity distribution thus accounts for the possibility of slip at the membrane surface, as well as the variation of the viscosity with temperature, given by [26]:

$$\mu(T) = 0.001\cdot\exp\left[-6.4313 + \frac{1882}{T}\right] \tag{6}$$

The boundary conditions for Eq. (2) are provided as follows:

$$\kappa\frac{\partial T}{\partial y}|_{y=0} = j\mathcal{L} \tag{7a}$$

$$T(x, y=\delta) = T_b \tag{7b}$$

$$T(x=0, y) = T_b \tag{7c}$$

where T_b is the temperature of the bulk fluid, κ is the liquid's thermal conductivity, δ is the boundary layer thickness, and $\mathcal{L}$ is the latent heat of evaporation.

The boundary condition (7a) states that all the heat required for the evaporation process is provided by conduction within the fluid phase. Conduction through the gas phase and membrane material is assumed to be negligible under reduced pressure conditions [1].

The vapor mass flux, j, is driven by the vapor pressure difference across the membrane, according to

$$j = B(P_{v,m} - P_0) \tag{8}$$

where $P_{v,m}$, P_0 denote the vapor pressure at the feed side membrane interface and the vacuum space, respectively. The coefficient B may be determined according to the mode of transport within the membrane pores. Vapor transport across the membrane has been successfully described by the dusty-gas model [1], which distinguishes between molecular diffusion (molecule–molecule collisions), Knudsen diffusion (molecule–wall collisions) and viscous flow (transport of a pure gas under a pressure gradient) as possible modes of transport. As a general rule, the mode of transport may be determined by calculating the Knudsen number, $Kn = \lambda/r$, representing the ratio of the pore radius, r, and the mean free path, λ, given by kinetic theory as:

$$\lambda = \frac{k_b T}{\sqrt{2}\pi\sigma^2 p} \tag{9}$$

with k_b denoting the Boltzmann constant and σ the molecular diameter (for water, $\sigma \approx 2.65$ Å). Eq. (9) predicts an increase in λ at reduced pressures; therefore, in a vacuum driven system with submicron pores ($r \simeq 0.2$ μm), the mean free path of the vapor may be well over an order of magnitude larger than the pore dimensions ($Kn >> 1$); moreover, it has been shown that for membranes with a pore radius smaller than 0.6 μm, the dominant transport mechanism may be assumed to be Knudsen diffusion [27]. In this case, the coefficient B may be expressed as [28]:

$$B = 1.064\frac{r\varepsilon}{\tau\delta_m}\left(\frac{M_w}{R_g T_a}\right)^{1/2} \tag{10}$$

where τ, δ_m and ε denote the membrane tortuosity, thickness and porosity, respectively, R_g is the universal gas constant, M_w is the vapor molecular mass and T_a is the average temperature within the pore.

The water vapor pressure at the interface may generally be approximated as the product of the water activity in the solution (concentration dependent) and the pure-water vapor pressure (temperature dependent):

$$P_v = a(\chi)P_v^0(T) \tag{11}$$

where $a(\chi)$ is the activity coefficient and χ is the solute mole fraction. The pure water vapor pressure and the activity coefficient may both be calculated using empirical correlations; the activity of a dilute solution may be approximated by Raoult's law, i.e.

$$a(\chi) = 1 - \chi \tag{12}$$

while the Antoine equation may be used to calculate the pure water vapor pressure at the liquid–gas interface, neglecting curvature effects:

$$P_v^0 = \exp\left(23.1964 - \frac{3816.44}{T - 46.13}\right) \tag{13}$$

In general, the vapor pressure exhibits a much weaker dependence on composition than on temperature. The following calculation illustrates this point; for an NaCl solution at an ambient temperature of 25 °C and concentration of 1 M, a 5% reduction of the vapor pressure would require a concentration increase of nearly 4-fold, while a similar decrease in vapor pressure would be obtained by lowering the temperature by ~1 °C. An accurate description of the concentration distribution and its effect on the process requires the coupled solution of Eq. (2) and an analogous mass balance equation. However, as this work is concerned with heat transfer, effects of mixture composition are ignored and only the temperature dependence is considered.

With the expression for the vapor pressure, the model of the feed channel heat transfer, coupled with evaporation through the membrane, is complete. In the following subsections, the solution methodology is outlined.

2.1. Integral method solution

Eq. (2), along with the boundary conditions (7), has no known analytical solutions and must be solved numerically. In what follows, we employ a semi-analytic, boundary-layer integral method which has been used for analysis of concentration polarization in ultrafiltration, and shown to be as accurate as a finite-difference scheme while being much less computationally intensive [29]. We assume the following versatile power-law temperature profile in the channel:

$$T(x,y) = T_b + (T_m(x) - T_b)\left(1 - \frac{y}{\delta(x)}\right)^{n(x)} \tag{14}$$

where T_m is the temperature at the membrane surface. In this form, the x dependance is contained within the functions $T_m(x)$, $\delta(x)$ and $n(x)$. The assumed profile is, in fact, a generalized form of the classical distribution used in the integral analysis of thermal and viscous boundary layers [25]; furthermore, it has been shown that distributions of this form match numerical simulations well [29].

Next, a moment technique is employed: the zeroth order moment is found by substituting the assumed profile (14) and its derivatives into Eq. (2) and integrating over the boundary layer thickness, resulting in the following equation:

$$\frac{2F_5}{\dot\gamma}\left(nK - \frac{j}{\rho}\delta\right) + \delta^3\frac{F_3}{F_2}\frac{dn}{dx} - \delta^2(F_1+4)\frac{d\delta}{dx} + \delta^3\frac{(F_1+2)}{(T_b - T_m)}\frac{dT_m}{dx} = 0 \tag{15}$$

where the following definitions have been made:

$$F_1 = \frac{(n+2)d_h l_0}{\delta}$$
$$F_2 = (n+1)(n+2)$$
$$F_3 = 2(F_1+3) + n(F_1+4)$$

A second equation is derived through the first order moment, obtained by multiplying Eq. (2) by y and again integrating across the boundary layer, upon substitution of the assumed profile and its derivatives:

$$\frac{2F_5}{\dot\gamma}\left(K - \frac{j}{\rho}\frac{\delta}{(n+1)}\right) + \delta^3\frac{F_6}{F_5}\frac{dn}{dx} - 2\delta^2(F_4+6)\frac{d\delta}{dx} + \delta^3\frac{(F_4+4)}{(T_b - T_m)}\frac{dT_m}{dx} = 0 \tag{16}$$

with

$$F_4 = \frac{(n+3)d_h l_0}{\delta}$$
$$F_5 = (n+3)F_2$$
$$F_6 = (n+3)(2n+3)F_4 + 4(3n^2 + 12n + 11)$$

A third equation is obtained by substituting the assumed temperature profile into the boundary condition (7a) and differentiating with respect to x, yielding:

$$\kappa(T_b - T_m)\frac{dn}{dx} + j\mathcal{L}\frac{d\delta}{dx} - (n\kappa + B\mathcal{L}\delta P_m'(T_m))\frac{dT_m}{dx} = 0 \tag{17}$$

where the prime denotes differentiation with respect to x.

The problem has thus been re-formulated into a system of three coupled ordinary differential equations, (15), (16) and (17), to be solved for the functions $T_m(x)$, $n(x)$ and $\delta(x)$.

2.2. Initial conditions

The inlet conditions (at $x = 0$) are, strictly speaking, that $T_m = T_b$ and $\delta = 0$; however, these conditions result in a singularity and so asymptotic conditions are found for the initiation of the numerical solution [29]. In Eqs. (15)–(17), we neglect all terms containing δ^3; subsequent solution of the simplified equations results in the following conditions:

$$\delta(x \to 0) = 2.7\left(\frac{xKd_h}{\dot\gamma}\right)^{1/3} \tag{18a}$$

$$n(x \to 0) = 3/2 \tag{18b}$$

The third initial condition is given implicitly by the equation:

$$2.7B\mathcal{L}\left(\frac{xKd_h}{\dot\gamma}\right)^{1/3}(P_0 - P_v(T_{m,0})) + \frac{3}{2}\kappa(T_b - T_{m,0}) = 0 \tag{18c}$$

where $T_m(x \to 0) = T_{m,0}$ denotes the asymptotic expression for the inlet temperature at the membrane surface, consistent with the conditions (18a) and (18b).

Table 1
Process parameters used in numerical calculations.

δ_m [μm]	τ [–]	ε [–]	r [μm]	d_h [mm]	L [m]	P_0 [pa]
150	2	0.7	0.2	2	0.5	2000

3. Results and discussion

The system of ODE's, Eqs. (15)–(17), is solved numerically by a fourth order Runge–Kutta routine. Initialization is made by choosing an arbitrarily small value of x ($x = 10^{-10}$ is used in the presented results), for which the initial values of T_m and δ are computed, using

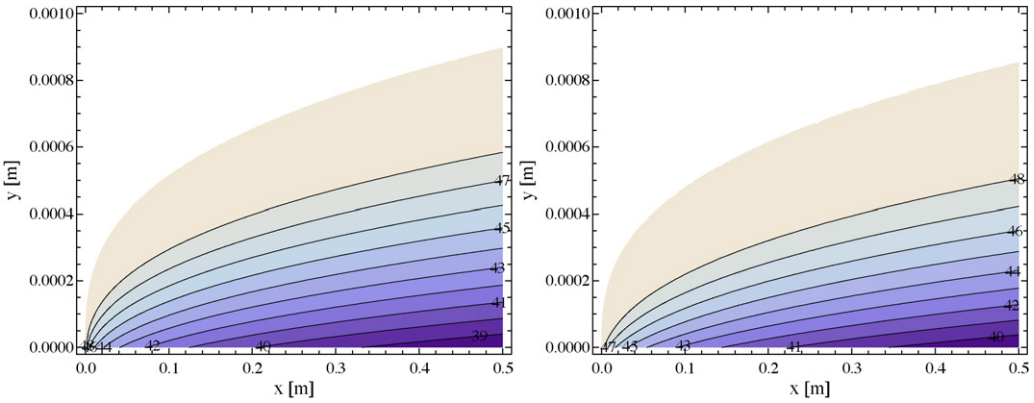

Fig. 3. Contours of the temperature field, $T(x, y)$, calculated with temperature variable viscosity, $\mu(T)$, at a bulk temperature of 50° C and a bulk velocity, $U = 0.5$ m/s. Left figure: no-slip ($l_0 = 0$). Right figure: $l_0 = 0.1$. Contour labels show the temperatures in °C, white regions are at the bulk temperature. Note that the outermost contour represents the edge of the thermal boundary layer.

Eqs. (18c) and (18a), respectively. Unless stated otherwise, values of the various parameters used in the computations are shown in Table 1. In the calculation of the coefficient B (Eq. (10)), the pore temperature T_a was estimated using the membrane surface temperature. Calculations have been made with varying values of the temperature and velocity, corresponding with Reynolds numbers ($Re = \rho U d_h/\mu$) in the range ≃300–2150.

The temperature field in the feed channel is shown in Fig. 3, calculated for the no-slip case as well as for an effective slip $l_0 = 0.1$. The features of the thermal boundary layer are clearly visible; the boundary layer thickness increases along the length of the channel (represented by the outermost contour, separating the bulk region (in white), from the thermal boundary layer). The surface temperature decreases in conjunction with the increase in the boundary layer thickness, as may be expected since evaporative cooling proceeds along the channel. When an effective slip is included in the calculation, the surface temperature is higher than in the corresponding no-slip case, and the boundary layer is, accordingly, thinner. This is indicative of a stronger axial convection under slip conditions. We also note, that in the illustrated calculations, the boundary layer has not yet reached its fully developed form (e.g. in a tube with $d_h = 2$ mm, or $R = 1$ mm, this means that $\delta < R$).

Fig. 4 shows the axial variation of the membrane surface temperature, calculated for different bulk temperatures, with and without accounting for viscosity changes. The observed deviation is more pronounced for higher bulk temperatures, since in this case the evaporation mass flux is higher, resulting in a stronger cooling at the interface. The increased evaporative cooling raises the viscosity, which in turn lowers the heat transfer rate; the combined effect is a higher degree of polarization. However, we note that within the range of parameters considered, inclusion of the viscosity temperature variations has a rather small effect; for example, the resulting difference in the channel-averaged evaporation mass flux is generally less than 4%.

Fig. 5 presents the effect of the bulk velocity on the channel-averaged membrane surface temperature, defined as:

$$\overline{T_m} = \frac{1}{L}\int_0^L T_m \, dx$$

The highest degree of polarization is predicted for the no-slip, variable viscosity case, while the inclusion of slip reduces the polarization even for a constant viscosity, and apparently has a stronger effect on the heat transfer. These results illustrate the contradicting effect imparted on the heat transfer by the two included mechanisms, namely velocity slip and variable viscosity. It is therefore conceivable that, at a certain slip coefficient, these effects will cancel each other and coincide with the no-slip, constant viscosity case (in terms of channel-averaged values). The case of variable viscosity and $l_0 = 0.04$ (dot-dashed curve in Fig. 5) illustrates this point: at low bulk velocities, the viscosity changes induce a higher polarization; however, as the velocity increases, this effect diminishes and the degree of polarization becomes lower than in the no-slip, constant viscosity case. In the final case presented, the highest degree

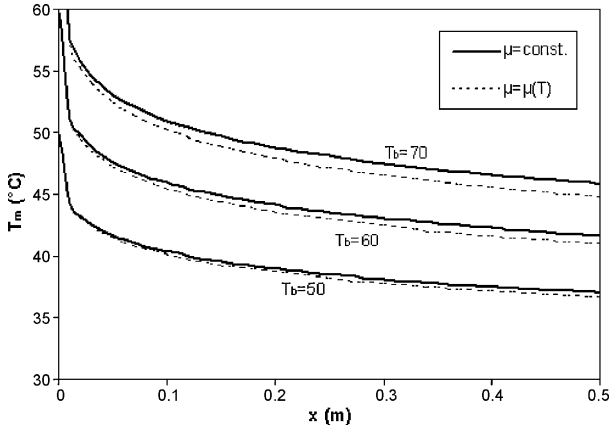

Fig. 4. Axial variation of membrane surface temperature, $T_m(x)$, illustrating the effect of temperature dependent viscosity. Calculations made with $U = 0.5$ m/s and $l_0 = 0$. Top curves, calculated for $T_b = 70$ °C: Solid— $\mu = const.$, Dashed— $\mu = \mu(T)$. Middle curves, calculated for $T_b = 60$ °C: Solid— $\mu = const.$, Dashed— $\mu = \mu(T)$. Bottom curves, calculated for $T_b = 50$ °C: Solid— $\mu = const.$, Dashed— $\mu = \mu(T)$.

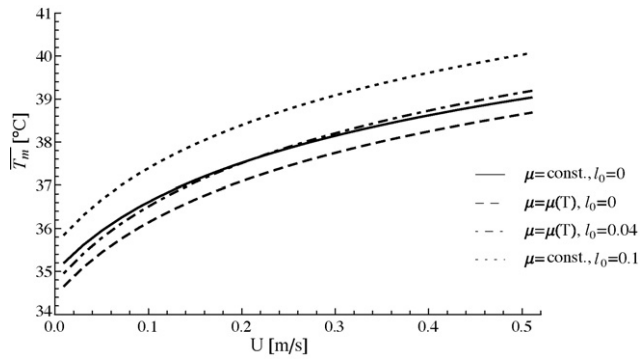

Fig. 5. Effect of the bulk velocity, U, on the channel-averaged, membrane surface temperature, $\overline{T_m}$, calculated for $T_b = 50$ °C: Solid curve— $\mu = const.$, no-slip ($l_0 = 0$). Dashed curve— $\mu = \mu(T)$, no-slip ($l_0 = 0$). Dot-dashed curve— $\mu = \mu(T)$, $l_0 = 0.04$. Dotted curve— $\mu = const.$, $l_0 = 0.1$.

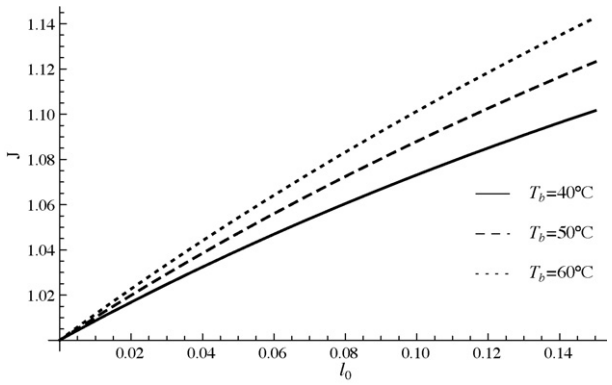

Fig. 6. Effect of the slip length, l_0, on the normalized channel-averaged evaporation mass flux, $J = \bar{j}/\bar{j}_0$, calculated with $U = 0.5$ m/s for various bulk temperatures. Solid curve— $T_b = 40\,^{\circ}$C. Dashed curve— $T_b = 50\,^{\circ}$C. Dotted curve— $T_b = 60\,^{\circ}$C. $\bar{j} = (1/L)\int_0^L j\,dx$ and $\bar{j}_0$ is the channel-averaged mass flux in the case where $l_0 = 0$ (no-slip).

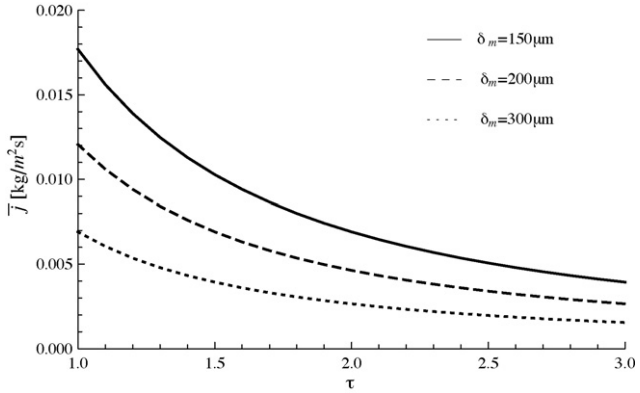

Fig. 7. Effect of the membrane tortuosity, τ, and thickness, δ_m, on the channel-averaged evaporation mass flux, $\bar{j}$. Calculations are made with a bulk temperature of $T_b = 50\,^{\circ}$C, bulk velocity $U = 0.5$ and $l_0 = 0$. Solid curve— $\delta_m = 150\,\mu$m. Dashed curve— $\delta_m = 200\,\mu$m. Dotted curve— $\delta_m = 300\,\mu$m.

of heat transfer is predicted when slip is accounted for, however the viscosity is constant.

The results described so far relate to the heat transfer characteristics and predicted variations of the temperature field in the feed channel, which is strongly coupled with the evaporation mass flux. The effect of velocity slip on the normalized channel-averaged mass flux, $J = \bar{j}/\bar{j}_0$, is depicted in Fig. 6, where the channel-averaged mass flux, $\bar{j}$, is defined as

$$\bar{j} = \frac{1}{L}\int_0^L j\,dx$$

and $\bar{j}_0$ is the channel-averaged mass flux in the case where $l_0 = 0$ (no-slip). The presence of velocity slip increases the evaporation mass flux, as may be anticipated from the results shown for the membrane surface temperature. The effect of velocity slip increases with the bulk temperature, which can again be explained as a greater relative reduction of temperature polarization. According to Eq. (5), the slip velocity increases with the bulk velocity, and is inversely proportional to the viscosity at the membrane surface. Therefore, slip effects become more pronounced at higher temperatures and bulk velocities. When the slip parameter is set as $l_0 = 0.1$ (equivalent to $l \approx 100\,\mu$m, with the parameters used in the presented calculations), the average mass flux is higher than the corresponding no-slip case by 5.6%, 8.8% and 10.2% at bulk temperatures of 40 °C, 50 ° C and 60 °C, respectively. The slip velocity at 50 ° C and $l_0 = 0.05$ would be 8.1 cm/s, or 16.2% of the bulk velocity (set at $U = 0.5$ m/s); this range of values is in accordance with some experimental observations of 'effective' slip on patterned hydrophobic surfaces, which measured slip velocities equal to 17% of the average velocity [20], ~15% of the maximum velocity [19,18] and slip lengths up to 30% of the flow channel dimensions [22].

The influence of membrane properties on the evaporation mass flux is also of interest. In particular, the tortuosity factor is difficult to quantify, and is often considered as an adjustable parameter in calculations. An ideal membrane would have a tortuosity of $\tau = 1$ (representing straight capillaries), and values of up to 3.9 have been reported in the literature [30]; however, a value of 2 is usually an acceptable approximation [31]. Calculations of the channel-averaged evaporation mass flux, $\bar{j}$, as a function of the membrane tortuosity and thickness, are shown in Fig. 7. Eq. (10) predicts that the evaporation mass flux is inversely proportional to the tortuosity and thickness, as indeed may be seen in Fig. 7. However, it is the combined effect of thickness and tortuosity which represents the effective length for trans-membrane transport; a thin membrane is far more sensitive to tortuosity variations, but equal fluxes are predicted for equal combinations of thickness and tortuosity.

As mentioned in a previous section, the transverse velocity component is induced by the evaporation at the interface, resulting in an additional convective mechanism transporting heat to the interface. Previous studies have made calculations based on film theory [8,32] and have estimated the relative contribution, in terms of the heat flux, to be 2–8% of the total heat flux. For comparison, the channel-averaged mass flux was calculated based on the procedure outlined in Section 2, however the transverse velocity component v was omitted from Eq. (2). The results are shown in Fig. 8, in terms of the parameter $\eta = 100 \times (\bar{j} - \tilde{j})/\bar{j}$, which represents the relative contribution of the channel averaged mass flux $\tilde{j}$, calculated without the transverse velocity, to $\bar{j}$ obtained by the corresponding full solution. The relative contribution increases with the bulk temperature, owing to the larger evaporation flux, and decreases at higher bulk velocities, since axial convection becomes increasingly dominant; however, under the range of parameters examined (up to 70 ° C and $U = 0.5$ m/s), the effect is not very significant (generally under 2%).

Finally, it is of interest to compare the predictions of the presented model with experimental results. To this end, calculations have been made using parameters corresponding with the experiments conducted in Ref. [10], listed in Table 2. The compared experimental results were obtained employing a capillary membrane bundle with the feed flowing in the lumen side and a vacuum applied in the shell side; pure water was used as feed, thus only

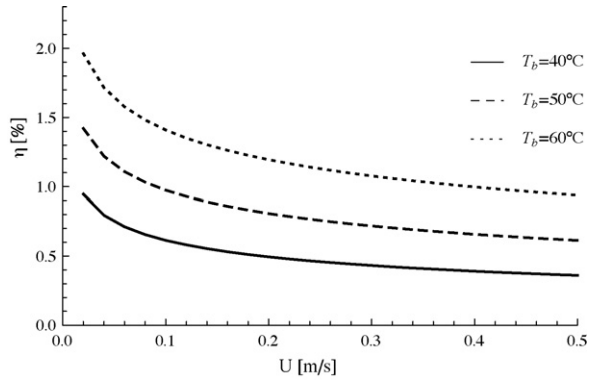

Fig. 8. Effect of the evaporation induced flow on the channel-averaged mass flux. Calculations shown in terms of the parameter η, which represents the % contribution of $\bar{j}$ (calculated without the transverse velocity component v), to the corresponding value of $\bar{j}$. Calculations are made for a varying bulk velocity and $l_0 = 0$. Solid curve— $T_b = 40\,^{\circ}$C. Dashed curve— $T_b = 50\,^{\circ}$C. Dotted curve— $T_b = 60\,^{\circ}$C.

Table 2
Parameters corresponding with experiments reported in Ref. [10].

δ_m [μm]	τ [–]	ε [–]	r [μm]	d_h [mm]	L [m]	P_0 [pa]
400	2	0.7	0.2	1.8	0.47	4000

temperature polarization effects are expected to exist. Fig. 9 shows calculations of the channel-averaged evaporation mass flux, plotted against the bulk velocity for various temperatures, compared with the experimental measurements. Calculations have been made accounting for variable viscosity, with and without the inclusion of velocity slip. Also shown are calculations made applying film theory, according to which the heat balance across the thermal boundary layer is given as:

$$j\mathcal{L} = h(T_b - T_m) \tag{19}$$

where h is the heat transfer coefficient, given by the following correlation [33]:

$$h = 1.86\left(RePr\frac{d_h}{L}\right)^{1/3}\left(\frac{\mu_b}{\mu_m}\right)^{0.14}\frac{\kappa}{d_h} \tag{20}$$

This correlation has been chosen primarily due to the fact that it is derived under hydrodynamic assumptions similar to those employed in our model formulation, while the boundary condition used is that of a constant wall temperature. This correlation is valid under laminar conditions ($Re < 2300$), and for values of $RePr(d_h/L) > 10$ [33]; these conditions are satisfied by the range of parameters used in the calculations. Film theory calculations were made using a mid-channel bulk temperature, estimated by assuming a linear temperature distribution and a temperature drop of ~3%; this represents a conservative case based on the range of measured inlet and outlet temperatures, reported in Ref. [10].

As may be seen, the model predictions are generally in good agreement with the experimental data. However, the inclusion of a slip velocity seems to offer better agreement, particularly at higher temperatures, where it has been shown that the slip effect becomes increasingly prominent. The calculations based on film theory noticeably under-predict the experimental data from Ref. [10]. While the use of heat transfer correlations has been criticized before, this serves to further illustrate the apparent difference between heat transfer at a constant-temperature solid boundary to that occurring at an evaporating liquid–gas interface, as is the case in the MD process. Furthermore, our results illustrate that a formulation which introduces a macroscopic 'effective' slip coefficient allows for a better agreement with measured data; the slip coefficient thus introduced may in fact be viewed as a 'lumped' parameter which accounts for micro-scale effects at the membrane surface. Such effects are likely to be present due to the flow and heat transfer occurring at a curved, evaporating gas–liquid interface supported by the membrane pores.

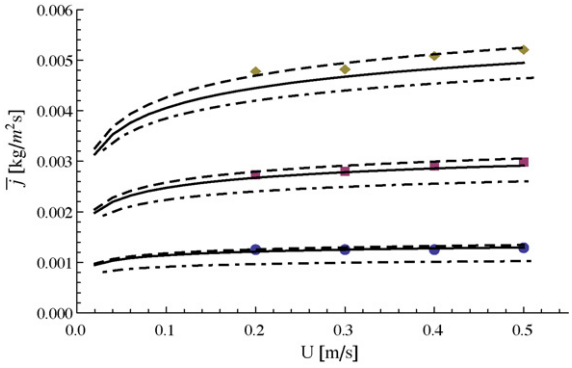

Fig. 9. Effect of the bulk velocity, U, on the channel averaged mass flux, $\bar{j}$. Solid curves calculated with no-slip ($l_0 = 0$), dashed curves calculated with $l_0 = 0.1$, dot-dashed curves represent calculations made using film theory with the heat transfer coefficient given by Eq. (20). Top curves calculated for $T_b = 60\,^\circ$C, middle curves calculated for $T_b = 50\,^\circ$C, bottom curves calculated for $T_b = 40\,^\circ$C. Points taken from experimental data of Ref. [10].

4. Summary and conclusion

A two-dimensional, boundary layer model is presented, for describing the heat transfer in the feed channel of a vacuum MD module. The model formulation allows for variations of viscosity with temperature, and introduces an 'effective' slip coefficient so as to account for the possible deviation of the flow and heat transfer characteristics over a liquid–gas interface, from those at a solid surface. The general integral method, introduced by De et al. [29], is used to reduce the computational complexity of the model equations. The results provide the temperature field in the feed channel and its dependence on the flow rate and bulk temperature. The effect of a temperature variable viscosity is shown to become increasingly important at higher temperatures, where a higher evaporative cooling increases the fluid's viscosity, resulting in a lower heat transfer rate and, consequently, a greater degree of polarization. In the presence of an 'effective' velocity slip, the degree of temperature polarization is reduced and a corresponding increase in the evaporation mass flux is observed. When the slip coefficient is set at $l_0 = 0.1$, the mass flux is increased by as much as 10.2%, at a bulk temperature of 60 ° C and bulk velocity of 0.5 m/s; at higher degrees of slip the flux is further increased. Calculated results are in good agreement with experimental data, in particular when velocity slip is accounted for; furthermore, the model predictions are in better agreement than calculations based on film theory with a heat transfer correlation, derived for heat exchange from a constant-temperature solid surface.

These results suggest that the flow field and resulting heat transfer characteristics over the alternating solid and gas interfaces encountered by the fluid should be accounted for, if accurate predictions are to be made. However, it should be noted that in the present study, the values used for the slip coefficient are estimated based on experiments conducted under a variety of conditions, none of which fully represents a micro-porous, hydrophobic membrane. It is therefore suggested that some experimentation be made, in order to more accurately assess the slip characteristics of an actual MD membrane. This will provide direct evidence, albeit macroscopic, of the existence and magnitude of an 'effective' slip coefficient. A simple procedure and equations, from which the effective slip parameter may be experimentally determined, are given in Appendix A.

Appendix A. Experimental evaluation of the effective slip parameter

In what follows, we briefly outline the equations and procedure for the experimental evaluation of the effective slip length in a cylindrical tube. The equation of motion for incompressible, steady, fully-developed flow in a cylindrical tube is given by

$$\frac{dp}{dz} = \frac{\mu}{r}\frac{d}{dr}\left(r\frac{du}{dr}\right) \tag{A.1}$$

where r and z are the radial and axial coordinates, respectively. This equation may be easily integrated, requiring that the velocity at the tube axis be finite and subject to the slip boundary condition

$$u(r = R) = l\frac{du}{dr}_{r=R} \tag{A.2}$$

where R denotes the tube radius. The solution is a modification of the well known Poiseuille flow:

$$u(r) = \frac{1}{4\mu}\frac{dp}{dz}(r^2 - R^2) + \frac{lR}{2\mu}\frac{dp}{dz} \tag{A.3}$$

where the second term on the right hand side represents the deviation from the Poiseuille distribution.

Two important quantities may be obtained from knowledge of the velocity distribution. The volumetric flow rate

$$Q = \int_0^R 2\pi r u(r)\,dr = -\frac{\pi}{2\mu}\frac{dp}{dz}R^4\left(\frac{1}{4} + \frac{l}{R}\right) \tag{A.4}$$

and the pressure drop,

$$\Delta P = \frac{2\mu\bar{u}L}{R^2\left((1/4) + (l/R)\right)} \tag{A.5}$$

with $\bar{u}$ denoting the cross-sectional average velocity.

Combining Eqs. (A.4) and (A.5), we obtain the following expression for the slip length:

$$l = \frac{2\mu L}{\pi R^3}\frac{Q}{\Delta P} - \frac{R}{4} \tag{A.6}$$

with this equation, the slip length may be calculated from measurements of the flow-rate and pressure drop across the length of the tube. Such a procedure has been successfully applied and shown to yield results which compare well with calculations based on direct measurements of the velocity distribution (see, for example, [19]).

Nomenclature

a	Water activity coefficient
B	Membrane distillation coefficient [kg m^{-2} s^{-1} pa^{-1}]
d_h	Hydraulic radius [m]
h	Heat transfer coefficient [J s^{-1} m^{-2} K^{-1}]
j	Evaporation mass flux [kg m^{-2} s^{-1}]
$\bar{j}$	Channel-averaged evaporation mass flux [kg m^{-2} s^{-1}]
$\tilde{j}$	Channel-averaged evaporation mass flux, calculated without transverse convection [kg m^{-2} s^{-1}]
$\overline{j_0}$	Channel-averaged evaporation mass flux in the case of a no-slip condition [kg m^{-2} s^{-1}]
J	Normalized evaporation mass flux, $\bar{j}/\overline{j_0}$
K	Thermal diffusivity [m^2 s^{-1}]
l	Slip length [m]
l_0	Scaled slip length, $2l/d_h$
L	Channel length [m]
$\mathcal{L}$	Latent heat of evaporation [J kg^{-1}]
M	Molar concentration [mole l^{-1}]
M_w	Molecular mass [kg mole^{-1}]
n	Exponent in power law distribution
$\hat{n}$	Unit normal vector
Pr	Prandtl number, ν/K
P_0	Pressure in vacuum space [pa]
P_ν	Vapor pressure [pa]
P_ν^0	Pure water vapor pressure [pa]
r	Membrane pore radius [m]
R	tube radius [m]
R_g	Gas constant [J mole^{-1} K^{-1}]
Re	Reynolds number, $\rho U d_h/\mu$
T	Temperature
u	Axial velocity component [m/s]
U	Bulk velocity [m/s]
v	Transverse velocity component [m/s]
$\vec{V}$	Velocity vector [m/s]

Greek letters

$\dot{\gamma}$	Shear rate, τ_w/μ_m [s^{-1}]
δ	Boundary layer thickness [m]
δ_m	Membrane thickness [m]
ε	Membrane porosity
η	% contribution of transverse convection to evaporation mass flux, $100 \times (\bar{j} - \tilde{j})/\bar{j}$
κ	Thermal conductivity [J m^{-1} s^{-1} K^{-1}]
λ	Mean free path [m]
μ	Viscosity [kg m^{-1} s^{-1}]
ν	Kinematic viscosity [m^2 s^{-1}]
ρ	Density [kg m^{-3}]
τ	Membrane tortuosity
τ_w	Wall shear stress [pa]
χ	Solute mole fraction

Subscripts

b	bulk
m	membrane
v	vapor

References

[1] K.W. Lawson, D.R. Lloyd, Membrane distillation, J. Membr. Sci. 124 (1) (1997) 1–25.
[2] Y. Yun, R. Ma, W. Zhang, A.G. Fane, J. Li, Direct contact membrane distillation mechanism for high concentration NaCl solutions, Desalination 188 (1–3) (2006) 251–262.
[3] M.T. Chan, A.G. Fane, J.T. Matheickal, R. Sheikholeslami, Membrane distillation crystallization of concentrated salts—flux and crystal formation, J. Membr. Sci. 257 (1–2) (2005) 144–155.
[4] J. Koschikowski, M. Wieghaus, M. Rommel, Solar thermal-driven desalination plants based on membrane distillation, Desalination 56 (1–3) (2003) 295–304.
[5] H.E.S. Fath, S.M. Elsherbiny, A.A. Hassan, M. Rommel, M. Wieghaus, J. Koschikowski, M. Vatansever, Pv and thermally driven small-scale, standalone solar desalination systems with very low maintenance needs, Desalination 225 (1–3) (2008) 58–69.
[6] L. Martinez-Diez, M.I. Vazquez-Gonzalez, F.J. Florido-Diaz, Temperature polarization coefficients in membrane distillation, Sep. Sci. Technol. 33 (6) (1998) 787–799.
[7] M. Gryta, M. Tomaszewska, Heat transport in the membrane distillation process, J. Membr. Sci. 44 (1–2) (1998) 211–222.
[8] J. Phattaranawik, R. Jiraratananon, A.G. Fane, Heat transport and membrane distillation coefficients in direct contact membrane distillation, J. Membr. Sci. 212 (1–2) (2003) 177–193.
[9] S. Srisurichan, R. Jiraratananon, A.G. Fane, Mass transfer mechanisms and transport resistances in direct contact membrane distillation process, J. Membr. Sci. 277 (1–2) (2006) 186–194.
[10] J.I. Mengual, M. Khayet, M.P. Godino, Heat and mass transfer in vacuum membrane distillation, Int. J. Heat Mass Transfer 47 (4) (2004) 865–875.
[11] A.M. Alklaibi, N. Lior, Transport analysis of air-gap membrane distillation, J. Membr. Sci. 255 (1–2) (2005) 239–253.
[12] S. Bouguecha, R. Chouikh, M. Dhahbi, Numerical study of the coupled heat and mass transfer in membrane distillation, Desalination 152 (1–3) (2003) 245–252.
[13] M.N. Chernyshov, G.W. Meindersma, A.B. de Haan, Modelling temperature and salt concentration distribution in membrane distillation feed channel, Desalination 157 (1–3) (2003) 315–324.
[14] C.L. Yaws (Ed.), Chemical Properties Handbook, McGraw-Hill, 1999.
[15] M. Khayet, M.P. Godino, J.I. Mengual, Study of asymmetric polarization in direct contact membrane distillation, Sep. Sci. Technol. 39 (1) (2004) 125–147.
[16] M. Qtaishat, T. Matsuura, B. Kruczek, M. Khayet, Heat and mass transfer analysis in direct contact membrane distillation, Desalination 219 (1–3) (2008) 272–292.
[17] C. Navier, Memoire sur les loir du mouvement des fluids, Memoires de l'Academie Royale des Sciences de l'Institut de France 6 (1823) 389–440.
[18] K. Watanabe, H. Yanuar, Mizunama, Slip of Newtonian fluids at solid boundaries, JSME Int. J. Series B 41 (3) (1998) 525–529.
[19] K. Watanabe, H. Yanuar, Mizunama, Drag reduction of Newtonian fluid in a circular pipe with highly water-repellent wall, J. Fluid Mech. 381 (1999) 225–238.
[20] J. Ou, J.P. Rothstein, Direct velocity measurements of the flow past drag-reducing ultrahydrophobic surfaces, Phys. Fluids 17 (10) (2005) 103606.1–103606.10.
[21] J. Ou, B. Perot, J.P. Rothstein, Laminar drag reduction in microchannels using ultrahydrophobic surfaces, Phys. Fluids 16 (12) (2004) 4635–4643.
[22] R. Truesdell, A. Mammoli, P. Vorobieff, F. Van Swol, C.J. Brinker, Drag reduction on a patterned superhydrophobic surface, Phys. Rev. Lett. 97 (4) (2006).

[23] M. Khayet, T. Matsuura, Pervaporation and vacuum membrane distillation processes: modeling and experiments, AIChE J. 50 (8) (2004) 1697–1712.
[24] A. Oron, S.H. Davis, S.G. Bankoff, Long scale evolution of thin liquid films, Rev. Mod. Phys. 69 (1997) 931–980.
[25] H. Schlichting, Boundary-layer Theory, 7th edition, McGraw-Hill, 1979.
[26] R.H. Perry, Perry's Chemical Engineer's Handbook, 6th edition, McGraw-Hill, 1990.
[27] L. Martinez, F.J. Florido-Diaz, A. Hernandez, P. Pradanos, Characterisation of three hydrophobic porous membranes used in membrane distillation: modelling and evaluation of their water vapour permeabilities, J. Membr. Sci. 203 (1–2) (2002) 15–27.
[28] R.W. Schofield, A.G. Fane, C.J.D. Fell, Heat and mass transfer in membrane distillation, J. Membr. Sci. 33 (3) (1987) 299–313.
[29] S. De, S. Bhattacharjee, A. Sharma, P. Bhattacharya, Generalized integral and similarity solutions of the concentration profiles for osmotic pressure controlled ultrafiltration, J. Membr. Sci. 130 (1997) 99–121.
[30] C. Ferandez-Pineda, M.C. Izquierdo-Gil, M.A. Garcia-Payo, Gas permeation and direct contact membrane distillation experiments and their analysis using different models, J. Membr. Sci. 198 (2002) 33–49.
[31] M.S. El-Bourawi, Z. Ding, R. Ma, M. Khayet, A framework for better understanding membrane distillation separation process, J. Membr. Sci. 285 (2006) 4–29.
[32] J. Phattaranawik, R. Jiraratananon, Direct contact membrane distillation: effect of mass transfer on heat transfer, J. Membr. Sci. 188 (1) (2001) 137–143.
[33] J.P. Holman, Heat Transfer, 6th edition, McGraw-Hill, 1986.